Journal of Power Sources 328 (2016) 46–55

Contents lists available at ScienceDirect

Journal of Power Sources

journal homepage: www.elsevier.com/locate/jpowsour

Analysis of geometric and electrochemical characteristics of lithium cobalt oxide electrode with different packing densities

Cheolwoong Lim [a], Bo Yan [a, b], Huixiao Kang [a], Zhibin Song [a], Wen Chao Lee [a], Vincent De Andrade [c], Francesco De Carlo [c], Leilei Yin [d], Youngsik Kim [e], Likun Zhu [a, *]

[a] Department of Mechanical Engineering, Indiana University–Purdue University Indianapolis, Indianapolis, IN, 46202, USA
[b] School of Materials Science and Engineering, Shanghai Jiao Tong University, Shanghai, 200030, China
[c] Advanced Photon Source, Argonne National Laboratory, Argonne, IL, 60439, USA
[d] Beckman Institute, University of Illinois, Urbana, IL, 61801, USA
[e] School of Energy & Chemical Engineering, Ulsan National Institute of Science and Technology (UNIST), Ulsan, Republic of Korea

GRAPHICAL ABSTRACT

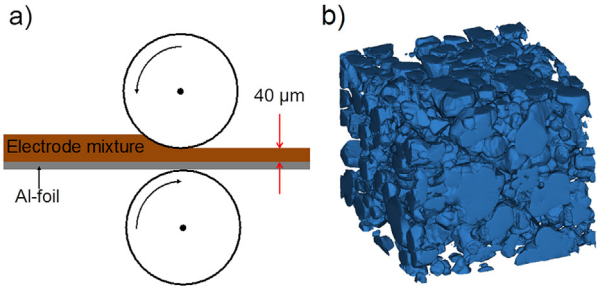

ARTICLE INFO

Article history:
Received 3 February 2016
Received in revised form
30 June 2016
Accepted 31 July 2016

Keywords:
Li ion battery
Synchrotron nano-computed tomography
Calendering
Packing density
Geometric characteristics

ABSTRACT

To investigate geometric and electrochemical characteristics of Li ion battery electrode with different packing densities, lithium cobalt oxide ($LiCoO_2$) cathode electrodes were fabricated from a 94:3:3 (wt%) mixture of $LiCoO_2$, polymeric binder, and super-P carbon black and calendered to different densities. A synchrotron X-ray nano-computed tomography system with a spatial resolution of 58.2 nm at the Advanced Photon Source of the Argonne National Laboratory was employed to obtain three dimensional morphology data of the electrodes. The morphology data were quantitatively analyzed to characterize their geometric properties, such as porosity, tortuosity, specific surface area, and pore size distribution. The geometric and electrochemical analysis reveal that high packing density electrodes have smaller average pore size and narrower pore size distribution, which improves the electrical contact between carbon-binder matrix and $LiCoO_2$ particles. The better contact improves the capacity and rate capability by reducing the possibility of electrically isolated $LiCoO_2$ particles and increasing the electrochemically active area. The results show that increase of packing density results in higher tortuosity, but electrochemically active area is more crucial to cell performance than tortuosity at up to 3.6 g/cm^3 packing density and 4 C rate.

* Corresponding author. Department of Mechanical Engineering, Indiana University Purdue University Indianapolis, 723 W. Michigan Street, Room SL 260 L, Indianapolis, IN, 46202, USA.
E-mail address: likzhu@iupui.edu (L. Zhu).

http://dx.doi.org/10.1016/j.jpowsour.2016.07.119
0378-7753/

1. Introduction

Over the last decade, rechargeable Li ion batteries (LIBs) have been widely utilized in portable electronics and become a popular power source for electric vehicles. The energy and power capabilities of LIBs have been considered crucial factors to determine the commercial values of the LIB powered applications. Many efforts have been done to improve the energy density and rate capability of LIBs. According to intrinsic material properties of anode and cathode active materials, high energy and power densities are achieved with high charge/discharge capacity, voltage and rate capability per unit mass or volume. In addition to material properties, the structure of electrode at micro and nano scales also plays a critical role in determining the energy density and rate capability of a LIB. Typically, a LIB electrode consists of active material, polymeric binder, and conductive carbon additive. The micron-sized active material particles are electrically connected via the nanometer-sized conductive carbon particles and maintained the mechanical integrity of the porous microstructure with polymeric binder. Using standard calendering process, present-day LIBs have ~50% of their volume occupied by the active materials [1,2]. Increased calendering can increase the packing density of active materials in LIB electrodes, thereby increasing the volumetric energy density. The specific energy density is also increased by calendering via decreasing the percentage of inactive materials, such as current collector and separator. However, higher fraction of active materials in LIB electrodes can change electrodes' structural properties significantly, such as porosity, specific surface area, pore size distribution and tortuosity. In addition, the packing density of active materials also can change the distribution of polymer binder and carbon additives in the porous microstructure of LIB electrodes [3]. These factors could have impacts on the performance of a LIB.

To this end, some research work has been conducted to study the calendering effect on electrochemical properties of LIB electrodes [4–6] and the impact of weight fraction of polymeric binder and conductive carbon additive on the performance of LIB electrodes [3]. For instance, Zheng et al. investigated calendering effects on the physical and electrochemical properties of $Li[Ni_{1/3}Mn_{1/3}Co_{1/3}]O_2$ (NMC) cathode [4,7]. They found that calendering improves the electrical conductivity between active material particles at relatively high porosities, but increases charge transfer resistance at electrode/electrolyte interface at relatively low porosities. van Bommel et al. investigated the effect of calendering $LiFePO_4$ electrodes and found that calendering resulted in a large decrease in contact resistance at the current collector - electrode interface and maintained their capacity better than uncalendered electrodes at high charge/discharge rates [5]. Haselrieder et al. studied the influence of the calendering process on surface morphology, mechanical, structural and electrochemical properties of graphite electrodes [8]. They found that the calendering doesn't have significant impact on power performance. Dahn et al. have reported the electrode compression effects on the LIB performance by enhancing the electrical connection of a low carbon contained cathode electrode [9]. Lai et al. reported a sintered binder-free lithium cobalt oxide ($LiCoO_2$) electrode with up to 87 vol% density for microscale applications [1]. Liu et al. introduced a physical model in which acetylene black and active material particles compete for polymer binder, which forms fixed layers of polymer on their surfaces [3].

However, there are few reports on the geometric characteristics and their impact on the electrochemical performance of LIB electrodes with different packing densities due to the inhomogeneity, complexity, and three-dimensional (3D) nature of the electrode's microstructure. The effects of geometric properties have been studied based on various mathematical models, such as particle size distribution [10,11], porosity distribution [12], and the contact resistance of various sizes of particles [13]. These models are based on the assumed homogeneous electrode microstructure or computer generated 3D electrode microstructures. Recently, porous electrode microstructures have been reconstructed by advanced tomography techniques such as X-ray nano-computed tomography (nano-CT) [14–20] and focused ion beam scanning electron microscope (FIB-SEM) [21–23]. The reconstructed microstructures have been employed to investigate the geometric characteristics and spatial inhomogeneity of porous electrodes [24–29]. Moreover, these techniques facilitated numerical studies of electrochemical systems by providing realistic microstructures [30–34]. By using synchrotron radiation X-ray tomographic microscopy, Ebner et al. studied the influence of compression and carbon black and binder content on NMC cathode electrode porosity and discharge capacity as a function of discharge rate [35]. However, more detailed geometric and electrochemical characteristics were not discussed in this report and the voxel size of the synchrotron radiation X-ray tomographic microscopy is $0.37 \times 0.37 \times 0.37\ \mu m^3$, which is relatively large if smaller active material particles are investigated.

Therefore, the purpose of this paper is to investigate the realistic geometric characteristics of $LiCoO_2$ cathode electrode microstructures with different packing densities and their impacts on electrochemical performance using synchrotron X-ray nano-CT technique with high spatial resolution. Although FIB-SEM tomography enables the detection of carbon-binder matrix, it was not chosen in this study due to the time consumption and difficulty of operation [30]. As mentioned earlier, the porous microstructure of LIB electrodes is dominated by the active and inactive materials and fabrication methods. In this study, $LiCoO_2$ was chosen as the model material and five $LiCoO_2$ electrodes were fabricated from a same composition of materials, and calendered to an identical thickness under different packing conditions. We reconstructed the porous microstructures of differently packed electrodes to examine geometric characteristics by employing synchrotron transmission X-ray microscopy (TXM) at the Advanced Photon Source (APS) of the Argonne National Laboratory (ANL). The electrodes were assembled in coin cells with a Li counter electrode for investigating the electrochemical characteristics. The fixed electrode thickness and material composition allow us to investigate the effects of packing density on the porous microstructure and electrochemical performance of $LiCoO_2$ electrodes.

2. Experimental

2.1. Materials

$LiCoO_2$ active material (99.5% 5 μm APS powder) was received from Alfa Aesar, Ward Hill, MA, super-P carbon black (C65, TIMCAL Ltd.) was from MTI, Richmond, CA, polyvinylidene difluoride (KF 1120 polymer − 12 wt % PVDF) binding agent was from Kureha, New York, NY, and *N*-methyl-2-pyrrolidinone solvent (NMP, anhydrous 99.5%) was from Sigma-Aldrich, St. Louis, MO, USA. EC/DEC Electrolyte containing 1 M $LiPF_6$ in a 1:1 volume-ratio mixture of ethylene carbonate and dimethyl carbonate was received from BASF, Elyria, OH, USA.

2.2. Electrode fabrications and cell assembly

The active material, binder, and carbon black current conductor (94:3:3 of weight ratio) were added in NMP solution. There are two reasons that we chose low carbon black and binder content in this study. The first one is that low carbon black and binder content can achieve high energy density which is very important in battery industry. The second one is that carbon black and binder cannot be

identified by synchrotron TXM and low content can help to reduce the 3D reconstruction error. The electrode slurry was mixed homogeneously by magnetic stir bar in a vial over 10 h. The gel-like slurry was coated onto a thin aluminum foil via a film casting doctor blade (EQ-Se-KTQ-100, MTI, Richmond, CA, USA). The doctor blade was pre-set to a certain thickness to ensure each electrode on the current collector has a uniform thickness. By controlling the setting of the doctor blade, five different thicknesses of cathode electrodes were coated on the current collector from 40 μm to 80 μm. Higher packing density electrodes (initial thickness higher than 80 μm) have also been tried using this method. However, the electrode always cracks after pressing. Due to this issue, the maximum initial thickness was set to 80 μm in this study. As shown in Ref. [9], the maximum packing density (3.6 g/cm^3) achieved in this study is comparable to that found in commercial electrodes. The electrodes were then dried under IR light around 0.5 h. These electrodes were pressed down to 40 μm using a rolling press machine (MR-100A, MTI, Richmond, CA, USA). A digital micrometer with 1 μm resolution (Digital micrometer-1IN/25MM, Marathon, Richmond Hill, ON, Canada) was used to measure the thickness of the electrodes. This method allows us to obtain five 40 μm electrodes with various packing densities. The electrodes were punched out in 8 mm diameter and dried in a vacuum oven at 110 °C for 10 h.

The five different packing density electrodes were assembled using standard 2016 coin cell hardware with a 16 mm diameter Li metal sheet as the counter electrode, Celgard 2400 separator, and the liquid electrolyte in an argon-filled glovebox (under O_2 < 0.1 ppm, H_2O < 0.1 ppm; Unilab 2000, Mbraun, Stratham, NH, USA). The cells were sealed using a compact hydraulic crimping machine (MSK-110, MTI, Richmond, CA, USA) and aged for 10 h before the first charge to ensure full absorption of electrolyte into the pores of the electrode.

Table 1 summarizes the control factors in electrode fabrication and their potential impacts on geometric/electrochemical properties and cell performance. The detailed discussions will be in the section of Results and discussion.

2.3. Electrochemical measurements

The prepared coin cells were initially cycled three times between 3.5 and 4.25 V (vs. Li/Li+) under a galvanostatic condition at 0.1 C rate before EIS measurements. AC impedance spectra were measured at different open circuit potential conditions using a two-electrode system with Li sheet as the counter electrode and $LiCoO_2$ as the working electrode (CHI660D, CH instrument, Austin, TX, USA). Since the AC impedance spectra were measured using a two-electrode system, the impedance is actually a combination of both $LiCoO_2$ working electrode and Li counter electrode. In order to investigate the influence of the impedance of Li electrode, Li/Li symmetric cells were constructed in the same coin cell setup and tested. The size of Li electrode is the same as the one in $LiCoO_2$ cells. The Li/Li cells were cycled three times at two different currents under a galvanostatic condition (1 cycle: 10 h charging and 10 h discharging) before EIS measurements. The high current is the same as the 0.1 C rate of the 3.6 g/cm^3 packing density electrode and the low current is slightly lower than the 0.1 C rate of the 2.2 g/cm^3 packing density electrode. The voltage amplitude was 5 mV, and the frequency range was between 1,000,000 Hz and 0.01 Hz. Equivalent circuit parameters were fitted to AC impedance spectra using the ZView fitting software. Moreover, the cells were charged and discharged for three cycles at each C rate from 0.1 C–4 C rates to investigate energy and power density changes (BT2000, Arbin, College Station, TX, USA).

2.4. Nano-CT data collection and image processing

The different packing density electrodes were soaked in 30% NaOH solution to remove the aluminum current collector. After the electrode samples were cleaned by DI water and dried in air, a sharp razor was used to break the samples to small pieces. Then one piece with a sharp wedge was selected and mounted to the rotation stage of the nano-CT system. A synchrotron TXM at beamline 32-ID-C at the APS of ANL was employed to obtain morphological data of the electrodes. High energy level X-ray (8 keV) from the beamline was able to capture the projected X-ray images with 2 s exposure time at each 0.25° rotation increments over 180°. Data collection was fully automated and the total collection time for one electrode sample was about 25 min.

The X-ray projected data were transformed to an image stack in Cartesian coordinate system using a python-based toolkit, Tomopy [36]. The resulting voxel size is 58.2 × 58.2 × 58.2 nm^3. To analyze the geometric characteristics, the aligned image stack was converted into 3D binary data using the Insight Toolkits (ITK) [37]. Tetrahedral meshed microstructures of the different packing density electrodes were generated from the binary volumetric data with iso2mesh MATLAB algorithm [38].

3. Results and discussion

The electrodes with different initial thicknesses were pressed down to 40 μm to achieve five different packing densities using the rolling press machine. Table S1 shows the various packing densities of the electrodes from 2.2 g/cm^3 to 3.6 g/cm^3. The calendering effect on the electrode structure is clearly shown in X-ray CT images (Fig. 1a and b). In the images, $LiCoO_2$ particles are shown as bright

Table 1
Summary of the control factors in electrode fabrication and their impacts on geometric/electrochemical properties and cell performance.

Control factors of electrode fabrication			
Packing density	Vary from 2.2 g/cm^3 to 3.6 g/cm^3		
Weight ratio of $LiCoO_2$, binder, and carbon black	94:3:3 wt%		
Thickness	40 μm		
Impacts of packing density on geometric/electrochemical properties and cell performance			
Change of geometric and electrochemical properties when packing density increases		Impact of the changes to the cell performance	
		Capacity	Rate capacity
Volumetric density of carbon and binder	Increase	+	
Porosity	Decrease	+	−
Specific surface area	Increase		
Tortuosity	Increase		−
Contact resistance	Decrease	+	+
Resistance of solid electrolyte interphase (SEI)	Decrease		+
Resistance of charge transfer	Decrease		+

color because of the high X-ray absorption of cobalt and the $LiCoO_2$ particles with 3.6 g/cm^3 density (Fig. 1b) are packed more densely than the one with 2.2 g/cm^3 density (Fig. 1a). The reconstructed microstructure of the 2.2 g/cm^3 electrode is shown in Fig. 1c. To validate the reconstructed electrode microstructures, the volume fractions of the electrode components based on reconstructed microstructure (Fig. 2a) are compared with the volume fractions based on the measured electrode weight and thickness (Fig. 2b). Due to the low X-ray absorption of PVDF binder and carbon conductor, they cannot be distinguished from the pore phase by the nano-CT system. In both Fig. 2a and b, the volume fractions of carbon conductor and PVDF binder phases are calculated based on their weight fractions (94:3:3) in the electrode and material densities ($LiCoO_2$ = 5.16 g/cm^3, carbon black = 2 g/cm^3, PVDF = 1.78 g/cm^3) [35]. A volume fraction of a material phase is the volume of the material over the total volume including all phases. The volume fractions of $LiCoO_2$ in the reconstructed microstructures increase with increasing packing density as well as the measured volume fractions. However, there are some variations (0.3%–4.9%) between Fig. 2a and b. The largest variation is 4.9% for the highest packing density electrode (ϕ = 3.6 g/cm^3). The variations can be explained by two reasons. First, the reconstructed volumes are around $30 \times 30 \times 30$ μm^3, which is limited by the field of view of the X-ray nano-CT and sample preparation. The active and inactive materials are randomly distributed in the electrodes. The reconstructed volume may not be large enough to quantify the volume fractions of the electrode. Second, the thickness of electrodes was measured by an electronic digital micrometer with 1 μm resolution. Since the total thickness is 40 μm, theoretically there is a 2.5% measuring error.

To investigate material distributions in the electrodes, pore size distribution was quantified from the 3D binary volume using the method described in our previous publication [28]. The pore size distribution results are shown in Fig. 3a. The minimum pore radius is 58.2 nm that is the same as the spatial resolution of the X-ray nano-CT. The relative volume is defined as the total volume of a pore radius over the volume of the inactive phases including carbon, PVDF, and pore phases. The pore radii are positively skewed for all electrodes and tend to concentrate at smaller radius range with the increased packing density. Fig. 3b shows box plots of pore radius of the different packing density electrodes. A box width is a range of pore radii from 25 to 75 percentiles and a centerline in the box indicates a median radius at a corresponding packing density. The median and box width are reduced with increasing packing density, which is in accord with the 2D nano-CT image results shown in Fig. 1a and b. For instance, the relative pore volume of 2.2 g/cm^3 electrode has the widest inter quartile range (box width = 0.93 μm) with the median radius 1.34 μm and the maximum radius 3.61 μm. The relative pore volume of 3.6 g/cm^3 electrode has the narrowest box width 0.7 μm with the median radius 0.76 μm and the maximum radius 2.44 μm. It is noted that there should be pores smaller than 58.2 nm that cannot be detected by the synchrotron TXM. As we can predict from distribution data shown in Fig. 3a, the relative volume of those small pores should be very small. Although the carbon and PVDF phases cannot be distinguished from the pore phase, the result still can relatively demonstrate that the calendering process by the rolling press contributes more homogeneous distributions of pores and carbon-binder matrix.

Specific surface area is the solid-electrolyte interface area of an electrode per bulk volume and is given by $3v_{LCO}/r$ under the homogeneous assumption, in which v_{LCO} is the volume fraction of the active material ($LiCoO_2$) and r is the radius of the spherical particle. In this study, the specific surface area can be obtained from the reconstructed microstructure. Fig. 4a shows similar results of packing density effect on the specific surface area of reconstructed microstructures and homogeneous electrodes with a radius of 2.5 μm. The specific surface area under homogeneous assumption is proportional with the packing density. In the homogenous case, the enlarged area does not significantly affect the interface reaction rate and C rate capability of LIBs since the corresponding current density is also proportional with the packing density. However, improved electrochemical performance of highly packed electrodes has been reported from many other groups [4,35,39,40]. Therefore, the reconstructed microstructures need to be investigated with other geometric characteristics that describe the irregular shaped particles, inhomogeneously distributed particles, and Li ion pathways. In addition, it should be noted that the specific surface area shown in Fig. 4a includes both the areas covered by carbon-binder matrix and open areas because the synchrotron TXM cannot distinguish carbon-binder phase from pore phase. In the following sections, we will show that these two different areas have an important impact on Li ion transport.

In the well-known Newman's model [42,43], effective diffusivity was introduced to solve the volume average Li ion transport equation for a porous electrode. It was given by

$$D_{eff} = D\frac{\varepsilon}{\tau} \quad (1)$$

where D is the Li ion diffusivity in electrolyte, ε is the porosity of the

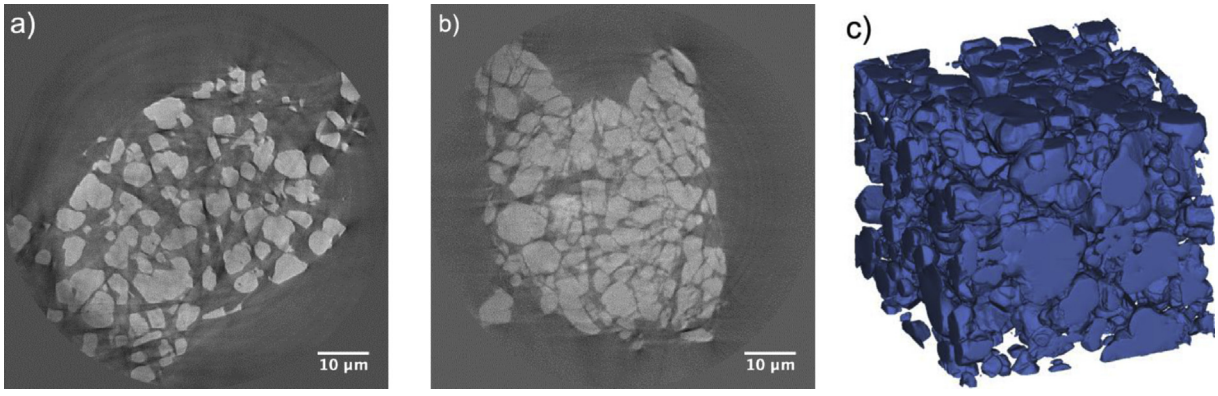

Fig. 1. 2D CT images of a) the lowest packing density electrode (2.2 g/cm^3) and b) the highest packing density electrode (3.6 g/cm^3) obtained by the synchrotron X-ray nano-CT. The bright color region represents $LiCoO_2$ particles. c) Reconstructed 3D microstructure of the lowest packing density electrode. (For interpretation of the references to colour in this figure legend, the reader is referred to the web version of this article.)

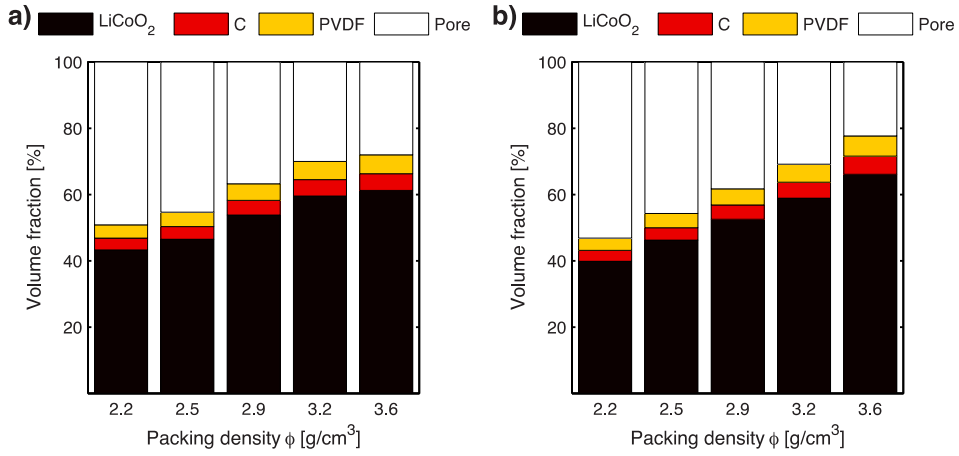

Fig. 2. Volume fractions of the electrode components calculated from a) the reconstructed porous microstructures and b) the loadings of the different packing density electrodes.

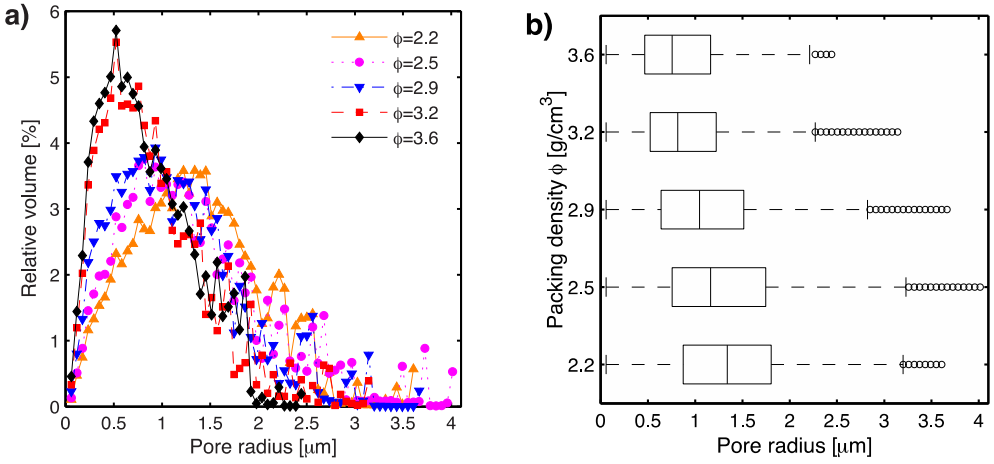

Fig. 3. a) Pore size distribution of the different packing density electrodes calculated from the reconstructed electrodes with the voxel size of 58.2 × 58.2 × 58.2 nm^3 and b) the corresponding box plot.

electrode, and τ is the tortuosity of the electrode. Tortuosity is considered as a function of porosity by Bruggeman relation ($\tau = \varepsilon^{0.5}$). Moreover, a numerical method has been proposed to calculate the tortuosity of a 3D inhomogeneous porous electrode by Kehrwald et al. [24]. They obtained the tortuosity by combining above definition of the effective diffusivity and mass flow rate in electrolyte geometry. Here, the porosity was considered as 1 minus volume fraction of $LiCoO_2$ of the reconstructed electrodes. Fig. 4b

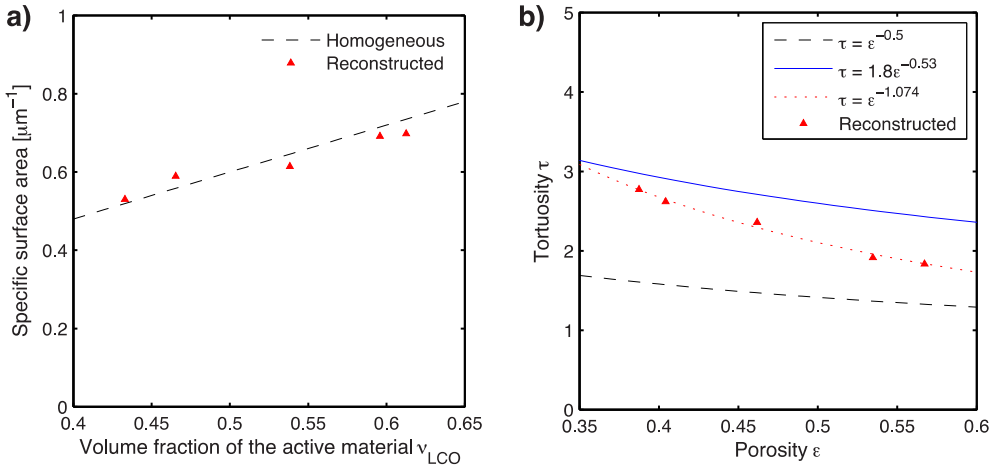

Fig. 4. a) Specific surface area of the reconstructed electrodes and the homogeneous electrodes with the different volume fraction of the active material. b) Tortuosity of the reconstructed electrodes compared with the Bruggeman relation and previously reported experimental results ($\tau = 1.8\varepsilon^{-0.53}$) [41].

shows the tortuosity results of the reconstructed electrodes with the corresponding porosity. The reconstructed tortuosity is between the Bruggeman relation and experimentally obtained tortuosity by Thorat et al. [41]. Based on the result, a fitting curve ($\tau = A\varepsilon^{1-\alpha}$) was estimated as a function of porosity and plotted in the figure (dotted red curve). In order to obtain accurate value for A, experiments similar to the one shown in Ref. [41] should be conducted. In this study, since we chose low carbon and binder content, the coefficient A was set as 1, and then the minimum tortuosity is 1 at porosity 1. It should be noted that the tortuosity is underestimated by neglecting carbon and binder effects. The root-mean-square error of the reconstructed tortuosity is 4.8% from the fit. The calculated tortuosity was lower than the Thorat's result in the given porosity range, but the reconstructed electrode shows sharp tortuosity increase at low porosity range. Whether the high tortuosity at high packing density will impact the Li ion transport in the electrode is one of the questions that we need to answer in this paper.

Under the homogeneous porous electrode assumption, geometric characteristics are easily obtained from the volume fractions of electrode components. Morphological effects on LIB performance can be estimated from numerical models that are originally developed by Newman's group. As previously mentioned, the inhomogeneity of electrode microstructure can give more insight to the cell performance. Therefore, in this study, electrochemical performance of differently packed $LiCoO_2$ electrodes was investigated with the quantified geometric characteristics. Fig. 5a shows charge-discharge profiles of the differently packed electrodes under a galvanostatic condition at 0.1 C rate. The C rates of the testing cells were calculated based on the weight of $LiCoO_2$ in the cathode electrodes that is noted in Table S1. The charge capacities are from 141 to 151 mA h/g, and the discharge capacities are from 140 to 148 mA h/g. From the specific capacities with respect to packing densities, we infer the existence of isolated $LiCoO_2$ particles in the low packing density electrodes [39]. The relatively small portion of carbon black (3 wt%) requires the closely packed electrode to electrically connect the active material particles. As shown in Fig. 1a and b, the distance between active material particles is reduced by the enhanced electrode calendering, and the smaller gap provides higher possibility to electrical connection of the particles. Fig. 5b shows discharge performance of the different packing density electrodes at 1 C rate. The increased packing density leads to higher discharge capacity at the higher C rate. Furthermore, the closely packed electrodes show higher discharge voltage profiles and better capacity retention at the all range of C rates (Fig. S1, Supporting Information).

The experimental results are summarized to describe the packing density effects on the cell performance at various discharge rates in Fig. 6. Fig. 6a shows discharge capacity retention of the electrodes from 0.1 C to 4 C discharge rate. For the most of C rates, the results show that the specific capacity increases with increased packing density. The unfilled markers at 0.1 C report the capacity retentions after 4 C rate tests. They are higher than 95% of the initial capacities showing the cells are not damaged with high rate cycling. As shown in Fig. 6b, the energy and power densities are described in the Rogone plot. It clearly shows the enhanced energy and power densities with increased packing density. As mentioned earlier, increase of packing density results in higher tortuosity (Fig. 4b), which has a negative impact on Li ion transport in electrolyte. This study shows that Li ion transport is not a limiting factor at up to 3.6 g/cm^3 packing density and 4 C rate. This result is in accord with the findings shown in Ref [1], which shows that Li ion transport in electrolyte is not rate-limiting when the porosity is lower than 75%. Furthermore, the calendering process did not break the $LiCoO_2$ particles to smaller ones as shown in Fig. 1b. We can assume that all the electrodes have similar particle size distribution and the particle size is not a factor to affect the electrochemical performance. As mentioned earlier, the capacity loss for low packing density cells at low C rates is caused by some electrically isolated particles. The large pore volume fraction and relatively large pore radii of low packing density electrodes demonstrate a high possibility of isolated particles. In addition, as mentioned in Ref. [4], high packing density electrode has higher breaking strength, which can avoid the shedding of active materials during battery processing and electrochemical cycling. This is another reason to explain the better specific capacity and rate capability of high packing density electrodes.

To further explain the effects of packing density on rate capability of the $LiCoO_2$ cathode electrodes, electrochemical impedance spectroscopy (EIS) tests were carried out after the initial 0.1 C galvanostatic cycles. The impedance response of the EIS tests at 4.25 V is reported in Fig. 7a. All the Nyquist plots of the five different packing density electrodes show two depressed semicircles as the frequencies progressed from high (left) to low (right). In the literature, the real-axis (Z′) intercept of a Nyquist plot at the high frequency has been assigned as the ohmic resistance of the cell (R_e) by the electrolyte [4]. The first semicircle in the high-to-mid frequency range has been ascribed to the resistance (R_{sf}) by the SEI layer formed on the active material [44] or the particle to particle interfacial contact resistance [4]. The second semicircle in the

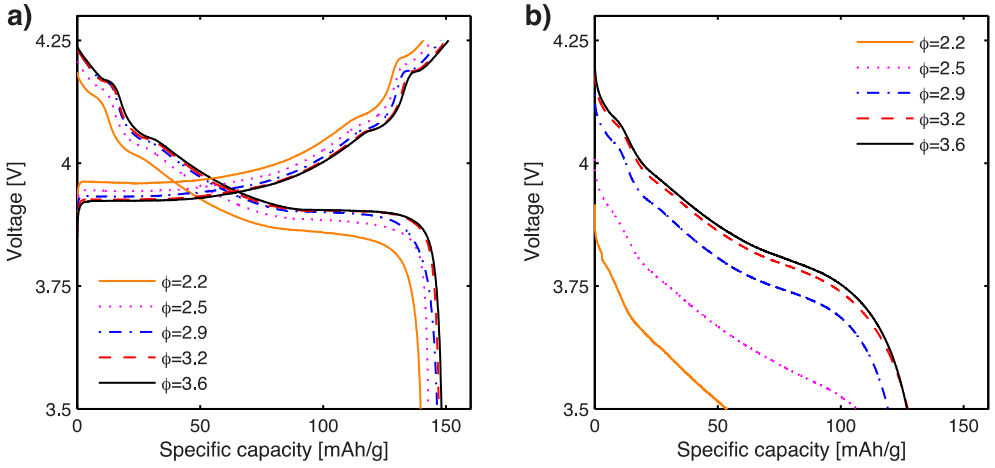

Fig. 5. Voltage profiles of the different packing density electrodes measured at a) 0.1 C rate and b) 1 C rate.

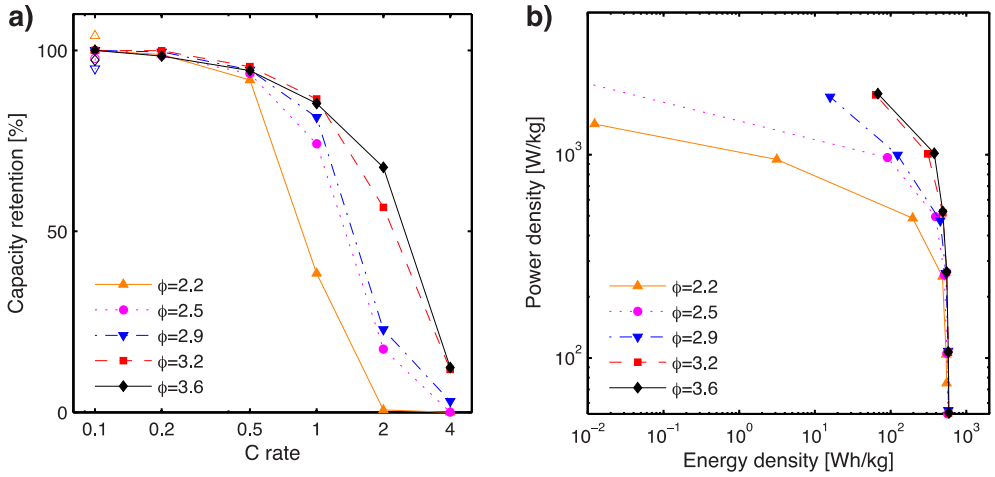

Fig. 6. Discharge performance of the different packing density electrodes summarized as a) Rate capabilities plot and b) Ragone plot.

mid-to-low-frequency range has been ascribed as the charge-transfer resistance (R_{ct}) at the electrolyte/electrode interface [45]. The Warburg type impedance response (Z_w) at the low frequencies has been considered as the solid-state diffusion of Li ions within the active material [45] and the electrolyte phase diffusion of Li ions [46]. Unlike Fig. 7a, the impedance responses at 3.5 V only show a single semicircle in the high-to-mid-frequency range (Fig. S2). The 3.2 g/cm^3 electrode cell was investigated to study the internal resistances at different cell potentials. The EIS measurement was conducted with a cell, which is stored for about two weeks after the

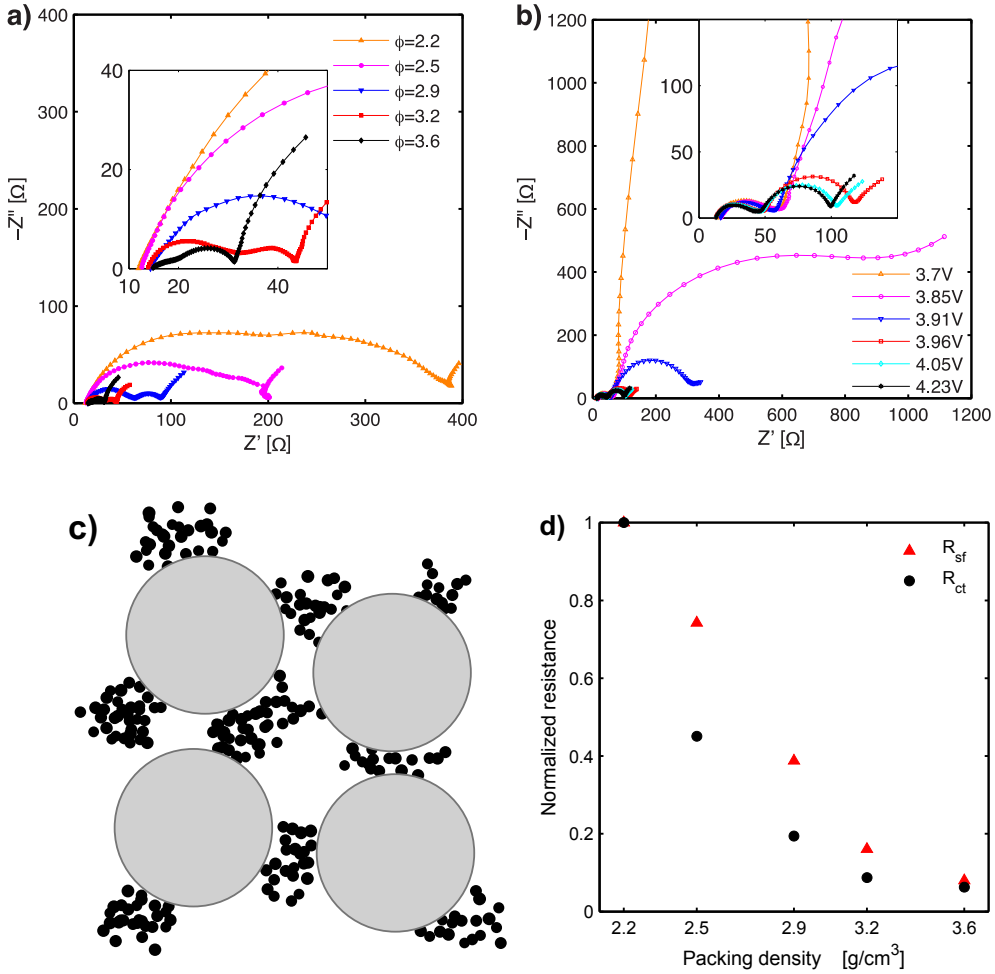

Fig. 7. AC impedance results plotted for a) the different packing density electrodes at 4.25 V and b) the 3.2 g/cm^3 electrode at various polarization voltages. c) Revised schematic of the aggregated carbon-binder matrix model [3]. d) Normalized internal resistances, R × mass/max(R × mass), in terms of the packing density.

rate capability testing. The impedance obtained from this cell should be relatively larger than the ones from the cell shown in Fig. 7a and b shows the measured Nyquit plots from 3.7 V to 4.23 V. The second semicircle is significantly reduced when the open circuit potential of the cell increased up to 3.96 V. It is because the large portion of Li (x) in the Li_xCoO_2 hinders the positive charge transfer at the electrode/electrolyte interface that causes a high R_{ct}.

In order to investigate the changes in the EIS spectra of $LiCoO_2$ electrodes with different packing densities in detail, we employed equivalent circuit displayed in Table 2 to analyze the impedance spectra data. As shown in Table 2, R_e is almost the same for all the electrodes with slightly larger value for high packing density electrodes and both R_{sf} and R_{ct} decrease significantly when the packing density increases. Fig. S3 shows the EIS spectra of two Li/Li symmetric cells. The equivalent circuit displayed in Table 2 was used to analyze the impedance spectra data. As shown in Table S2, the R_{sf} from the Li electrode for the R_{sf} data shown in Table 2 should be between 1.7 Ω and 4.35 Ω, and the R_{ct} from the Li electrode for the R_{ct} data shown in Table 2 should be between 7.9 Ω and 14.35 Ω. Both impedances increase as the cycling current (packing density) decreases. It should be noted that the R_{sf} and R_{ct} of one Li electrode should be 50% of the impedance value shown in Table S2, because the Li/Li symmetric cells have two identical Li electrodes. As shown in Tables 2 and S2, the R_{ct} impedance of Li electrode count for a large portion of the total impedance for high packing density cells, such as the 3.6 g/cm^3 cell. However, the contribution of the R_{ct} impedance of Li electrode is very small for low packing density cells. The contribution of the R_{sf} impedance of Li electrode is generally small for all the packing densities. If we take the impedance of Li electrode into account, the trend of R_{sf} and R_{ct} of the $LiCoO_2$ electrodes is still the same. The R_{sf} and R_{ct} decrease significantly when the packing density increases.

To explain the trend of R_{sf} and R_{ct} with packing density, we would like to introduce a schematic (Fig. 7c) of a composite electrode that contains a large portion of active material [3]. The schematic describes the distribution of conductive carbon-binder matrix in the composite electrode, when the carbon black to PVDF ratio is high and the active material loading is higher than 73%. This model is well supported by the SEM images of our electrodes shown in Fig. S4. Ref. [3] shows that the carbon aggregation causes limited contact area between the conductive matrix and active material surfaces. The limited contact area reduces the overall area that is electrochemically active for Li ion insertion and removal. As shown in Figs. 2 and 3, high packing density electrode has higher binder volumetric density, smaller porosity and smaller/narrower pore size distribution. We believe that these geometric features cause more uniform distribution of conductive carbon-binder matrix and better contact between carbon-binder matrix and $LiCoO_2$ particles. The contact area between carbon-binder matrix and $LiCoO_2$ particles is higher, thereby leading to the increase of electrochemically active area. Therefore, the charge transfer resistance (R_{ct}) is reduced in high packing density electrodes. The increase of electrochemically active area can also be used to explain the R_{sf} results if it is ascribed to the resistance of SEI layer. Because SEI layer usually forms on the electrochemically active area, the high packing density electrode with larger electrochemically active area has more SEI layer formed, which causes lower R_{sf}. However, in the literature, different mechanisms have been proposed for R_{sf}. One of the possible resistances is the resistance associated with the electronic properties of $LiCoO_2$ particles. Qiu et al. have shown that this resistance appears in the middle frequency region and sometimes overlaps with the SEI layer resistance in the EIS Nyquist plots [47]. They also show that the resistance due to electronic properties of $LiCoO_2$ particles changes dramatically in the charge/discharge process, which is agreement with previous reports that the electrical conductivity of $LiCoO_2$ changes one or two orders of magnitude in the charge/discharge process [48,49]. However, our results of the 3.2 g/cm^3 electrode show that R_{sf} only increases from 32.3 Ω to 48.6 Ω when the polarization voltage is decreased from 4.23 V to 3.7 V (Table S3). Another possible resistance is the resistance associated with the active material particle to particle interfacial contact resistance proposed by Zheng et al. [4]. They drew this conclusion because this resistance is significantly affected by the physical property of the electrode, including the chemical composition, electrical conductivity and porosity. However, this conclusion means that electrons transport through $LiCoO_2$ particles to participate the electrochemical reaction on the active material particle/electrolyte interface. Then the resistance associated with the electronic properties of $LiCoO_2$ particles should appear in the EIS data and change dramatically in the charge/discharge process. This phenomenon does not appear in our EIS data (Fig. 7b). The contact resistance could be also from the contact between current collector and electrode [50,51]. However, this resistance should be relatively stable during the charge/discharge process, which cannot interpret the resistance change at different state of discharge shown in Fig. 7b.

To explain the EIS data shown in Fig. 7a and b, we propose a model for electron transport and Li ion insertion/deinsertion in the composite electrode and associate R_{sf} to the SEI layer resistance. The electrical contact between the $LiCoO_2$ particle and the carbon/binder matrix is the main reason for SEI layer change with different packing density electrodes. In this model, the carbon/binder matrix is a nano porous structure and is conductive for both Li ion and electrons. Li ion transports through the pores of the porous carbon/binder matrix. The contact area forms electrochemically active sites and SEI layers will form on those sites during initial cell cycling for Li ion insertion/deinsertion reaction. The electrons only transport

Table 2
Internal resistances of the different packing density electrodes at 4.25 V and the equivalent circuit.

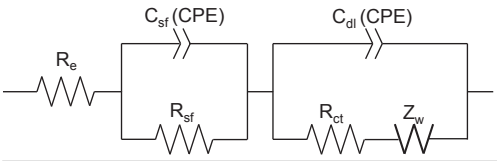

Packing density [g/cm^3]	R_e [Ω]	R_e error [%]	R_{sf} [Ω]	R_{sf} error [%]	R_{ct} [Ω]	R_{ct} error [%]
2.2	11.9	1.2	143.1	9.1	233.5	6.2
2.5	12.4	1.2	93.5	13.6	92.6	25.2
2.9	14.7	0.9	42.1	3.4	34.4	11.3
3.2	13.7	1.0	15.8	3.5	14.0	4.5
3.6	14.7	1.4	7.0	13.4	9.0	8.5

through the carbon/binder matrix in the composite electrode to the electrochemically active sites to participate electrochemical reactions. The electrochemically active area between $LiCoO_2$ particle and carbon/binder matrix is directly related to the R_{sf} resistance. As shown in Fig. 7c, the high packing density could enhance the interfacial contact between the active particles and carbon-binder matrix, which means reduced R_{sf} and R_{ct}. Moreover, as shown in Fig. 7b, lowering the state of discharge (x) reduces R_{sf}. This phenomenon has been commonly attributed to the reversible breakdown or dissolution of SEI films at higher voltages [52].

Fig. 7d shows normalized internal resistances at the corresponding packing densities. The resistances (R_{sf} and R_{ct}) of the electrodes in Table 2 were multiplied with their loading and divided by the maximum values (the resistances of the 2.2 g/cm^3 electrode). Levi et al. reported that R_{ct} is inversely proportional to the exchange current density [44]. For the different packing density cells, the electrochemically active area is the only variable to define the exchange current densities at the same cell voltage. The difference of the total surface area by the loadings was already removed for the normalized R_{ct} by multiplying the loading. Both the normalized R_{ct} and R_{sf} show an inversely proportional relationship with the packing density. The normalized R_{sf} could also be impacted by the non-uniform thickness of SEI layer on the electrochemically active area and involvement of some contact resistance. These results support the claim that enhanced packing density improves the electric network of the electrode as well as enlarging the electrochemically active area.

4. Conclusions

Geometric characteristics of $LiCoO_2$ electrode microstructures containing 3 wt% carbon black and 3 wt% PVDF with different packing densities and their impacts on electrochemical performance were investigated in this study. The realistic 3D microstructure of $LiCoO_2$ electrodes with voxel size of $58.2 \times 58.2 \times 58.2$ nm^3 were obtained using the synchrotron TXM at beamline 32-ID-C at the APS of ANL. The geometric analysis shows that high packing density can result in smaller pore size and more uniform pore size distribution. Without considering the effect of polymeric binder and carbon black, the specific surface area shows the linear relation with packing density and the tortuosity increases with increasing packing density. The electrode with higher packing density shows larger capacity, rate capability, energy density and power density. The larger capacity could be due to the less isolated $LiCoO_2$ particles and enhanced electrical connection of the electrode at high packing density. The EIS results show that the SEI layer resistance and the charge transfer resistance decrease with increasing packing density. The smaller pore size and uniform pore distribution cause more uniform distribution of conductive carbon-binder matrix and better contact between carbon-binder matrix and $LiCoO_2$ particles, which lead to the increase of electrochemically active area. Thus, the internal resistances are reduced in the high packing density electrodes. The tortuosity analysis and experimental results demonstrate that the electrochemically active area is more crucial than electrolyte phase Li ion transport to the cell performance at up to 3.6 g/cm^3 packing density and 4 C rate.

Acknowledgments

This work was supported by US National Science Foundation under Grant No. 1335850 and used resources of the Advanced Photon Source, a U.S. Department of Energy (DOE) Office of Science User Facility operated for the DOE Office of Science by Argonne National Laboratory under Contract No. DE-AC02-06CH11357. We thank Prof. Yongzhu Fu and Dr. Yadong Liu at IUPUI for helpful discussions about the electrochemical performance analysis.

Appendix A. Supplementary data

Supplementary data related to this article can be found at http://dx.doi.org/10.1016/j.jpowsour.2016.07.119.

References

[1] W. Lai, C.K. Erdonmez, T.F. Marinis, C.K. Bjune, N.J. Dudney, F. Xu, R. Wartena, Y.M. Chiang, Adv. Mater. 22 (2010) E139–E144.
[2] X. Qin, X. Wang, J. Xie, L. Wen, J. Mater. Chem. 21 (2011) 12444–12448.
[3] G. Liu, H. Zheng, X. Song, V.S. Battaglia, J. Electrochem. Soc. 159 (2012) A214–A221.
[4] H. Zheng, L. Tan, G. Liu, X. Song, V.S. Battaglia, J. Power Sources 208 (2012) 52–57.
[5] A. van Bommel, R. Divigalpitiya, J. Electrochem. Soc. 159 (2012) A1791–A1795.
[6] G.-F. Yang, S.-K. Joo, Electrochim. Acta 170 (2015) 263–268.
[7] H. Zheng, G. Liu, X. Song, P. Ridgway, S. Xun, V.S. Battaglia, J. Electrochem. Soc. 157 (2010) A1060–A1066.
[8] W. Haselrieder, S. Ivanov, D.K. Christen, H. Bockholt, A. Kwade, ECS Trans. 50 (2013) 59–70.
[9] T. Marks, S. Trussler, A. Smith, D. Xiong, J. Dahn, J. Electrochem. Soc. 158 (2011) A51–A57.
[10] R. Darling, J. Newman, J. Electrochem. Soc. 144 (1997) 4201–4208.
[11] G.S. Nagarajan, J. Van Zee, R. Spotnitz, J. Electrochem. Soc. 145 (1998) 771–779.
[12] V. Ramadesigan, R.N. Methekar, F. Latinwo, R.D. Braatz, V.R. Subramanian, J. Electrochem. Soc. 157 (2010) A1328–A1334.
[13] D.E. Stephenson, E.M. Hartman, J.N. Harb, D.R. Wheeler, J. Electrochem. Soc. 154 (2007) A1146–A1155.
[14] P. Shearing, L. Howard, P.S. Jørgensen, N. Brandon, S. Harris, Electrochem. Commun. 12 (2010) 374–377.
[15] R. Thiedmann, O. Stenzel, A. Spettl, P.R. Shearing, S.J. Harris, N.P. Brandon, V. Schmidt, Comput. Mater. Sci. 50 (2011) 3365–3376.
[16] C. Lim, B. Yan, L. Yin, L. Zhu, Electrochim. Acta 75 (2012) 279–287.
[17] Y.-c.K. Chen-Wiegart, P. Shearing, Q. Yuan, A. Tkachuk, J. Wang, Electrochem. Commun. 21 (2012) 58–61.
[18] Y.-c.K. Chen-Wiegart, Z. Liu, K.T. Faber, S.A. Barnett, J. Wang, Electrochem. Commun. 28 (2013) 127–130.
[19] S. Cooper, D. Eastwood, J. Gelb, G. Damblanc, D. Brett, R. Bradley, P. Withers, P. Lee, A. Marquis, N. Brandon, J. Power Sources 247 (2014) 1033–1039.
[20] S.K. Babu, A.I. Mohamed, J.F. Whitacre, S. Litster, J. Power Sources 283 (2015) 314–319.
[21] T. Hutzenlaub, S. Thiele, R. Zengerle, C. Ziegler, Electrochem. Solid-State Lett. 15 (2011) A33–A36.
[22] J.R. Wilson, J.S. Cronin, S.A. Barnett, S.J. Harris, J. Power Sources 196 (2011) 3443–3447.
[23] Z. Liu, J.S. Cronin, K. Yu-chen, J.R. Wilson, K.J. Yakal-Kremski, J. Wang, K.T. Faber, S.A. Barnett, J. Power Sources 227 (2013) 267–274.
[24] D. Kehrwald, P.R. Shearing, N.P. Brandon, P.K. Sinha, S.J. Harris, J. Electrochem. Soc. 158 (2011) A1393–A1399.
[25] M. Ender, J. Joos, T. Carraro, E. Ivers-Tiffée, J. Electrochem. Soc. 159 (2012) A972–A980.
[26] P. Shearing, N. Brandon, J. Gelb, R. Bradley, P. Withers, A. Marquis, S. Cooper, S. Harris, J. Electrochem. Soc. 159 (2012) A1023–A1027.
[27] M. Ebner, F. Marone, M. Stampanoni, V. Wood, Science 342 (2013) 716–720.
[28] C. Lim, B. Yan, L. Yin, L. Zhu, Energies 7 (2014) 2558–2572.
[29] L. Zielke, T. Hutzenlaub, D.R. Wheeler, C.W. Chao, I. Manke, A. Hilger, N. Paust, R. Zengerle, S. Thiele, Adv. Energy Mater. 5 (2015).
[30] D.E. Stephenson, B.C. Walker, C.B. Skelton, E.P. Gorzkowski, D.J. Rowenhorst, D.R. Wheeler, J. Electrochem. Soc. 158 (2011) A781–A789.
[31] B. Yan, C. Lim, L. Yin, L. Zhu, J. Electrochem. Soc. 159 (2012) A1604–A1614.
[32] A.H. Wiedemann, G.M. Goldin, S.A. Barnett, H. Zhu, R.J. Kee, Electrochim. Acta 88 (2013) 580–588.
[33] B. Yan, C. Lim, L. Yin, L. Zhu, Electrochim. Acta 100 (2013) 171–179.
[34] B. Yan, C. Lim, Z. Song, L. Zhu, Electrochim. Acta 185 (2015) 125–141.
[35] M. Ebner, F. Geldmacher, F. Marone, M. Stampanoni, V. Wood, Adv. Energy Mater. 3 (2013) 845–850.
[36] D. Gursoy, F. De Carlo, X. Xiao, C. Jacobsen, J. Synchrotron Rad. 21 (2014) 1188–1193.
[37] L. Ibanez, W. Schroeder, L. Ng, J. Cates, The ITK Software Guide, third ed., 2003.
[38] Q. Fang, D.A. Boas, Biomedical imaging: from nano to mmacro, in: ISBI '09. IEEE International Symposium on, 2009, 2009, pp. 1142–1145.
[39] J. Gnanaraj, Y.S. Cohen, M. Levi, D. Aurbach, J. Electroanal. Chem. 516 (2001) 89–102.
[40] J. Shim, K.A. Striebel, J. Power Sources 119 (2003) 934–937.
[41] I.V. Thorat, D.E. Stephenson, N.A. Zacharias, K. Zaghib, J.N. Harb, D.R. Wheeler, J. Power Sources 188 (2009) 592–600.
[42] M. Doyle, T.F. Fuller, J. Newman, J. Electrochem. Soc. 140 (1993) 1526–1533.

[43] M. Doyle, J. Newman, Electrochim. Acta 40 (1995) 2191–2196.
[44] M. Levi, G. Salitra, B. Markovsky, H. Teller, D. Aurbach, U. Heider, L. Heider, J. Electrochem. Soc. 146 (1999) 1279–1289.
[45] M. Thomas, P. Bruce, J. Goodenough, J. Electrochem. Soc. 132 (1985) 1521–1528.
[46] J. Huang, Z. Li, J.B. Zhang, S.L. Song, Z.L. Lou, N.N. Wu, J. Electrochem. Soc. 162 (2015) A585–A595.
[47] X.-Y. Qiu, Q.-C. Zhuang, Q.-Q. Zhang, R. Cao, P.-Z. Ying, Y.-H. Qiang, S.-G. Sun, PCCP 14 (2012) 2617–2630.
[48] M. Park, X. Zhang, M. Chung, G.B. Less, A.M. Sastry, J. Power Sources 195 (2010) 7904–7929.
[49] J. Barker, R. Pynenburg, R. Koksbang, M. Saidi, Electrochim. Acta 41 (1996) 2481–2488.
[50] M. Gaberscek, J. Moskon, B. Erjavec, R. Dominko, J. Jamnik, Electrochem. Solid State Lett. 11 (2008) A170–A174.
[51] J. Illig, M. Ender, T. Chrobak, J.P. Schmidt, D. Klotz, E. Ivers-Tiffee, J. Electrochem. Soc. 159 (2012) A952–A960.
[52] S.S. Zhang, K. Xu, T.R. Jow, J. Electrochem. Soc. 149 (2002) A1521–A1526.